Systematic study of target localization for bioluminescence tomography guided radiation therapy

Jingjing Yu[a)]
Department of Radiation Oncology and Molecular Radiation Sciences, Johns Hopkins University, Baltimore, Maryland 21231 and School of Physics and Information Technology, Shaanxi Normal University, Shaanxi 710119, China

Bin Zhang[a)]
Department of Radiation Oncology and Molecular Radiation Sciences, Johns Hopkins University, Baltimore, Maryland 21231

Iulian I. Iordachita
Laboratory for Computational Sensing and Robotics, Johns Hopkins University, Baltimore, Maryland 21218

Juvenal Reyes
Department of Radiation Oncology and Molecular Radiation Sciences, Johns Hopkins University, Baltimore, Maryland 21231

Zhihao Lu
Department of Oncology and Department of Surgery, Johns Hopkins University, Baltimore, Maryland 21231 and Key laboratory of Carcinogenesis and Translational Research, Department of GI Oncology, Peking University, Beijing Cancer Hospital and Institute, Beijing 100142, China

Malcolm V. Brock
Department of Oncology and Department of Surgery, Johns Hopkins University, Baltimore, Maryland 21231

Michael S. Patterson
Department of Medical Physics and Applied Radiation Sciences, McMaster University, Hamilton, Ontario L8S 4L8, Canada

John W. Wong and Ken Kang-Hsin Wang[b)]
Department of Radiation Oncology and Molecular Radiation Sciences, Johns Hopkins University, Baltimore, Maryland 21231

(Received 23 November 2015; revised 8 April 2016; accepted for publication 11 April 2016; published 2 May 2016)

Purpose: To overcome the limitation of CT/cone-beam CT (CBCT) in guiding radiation for soft tissue targets, the authors developed a spectrally resolved bioluminescence tomography (BLT) system for the small animal radiation research platform. The authors systematically assessed the performance of the BLT system in terms of target localization and the ability to resolve two neighboring sources in simulations, tissue-mimicking phantom, and *in vivo* environments.

Methods: Multispectral measurements acquired in a single projection were used for the BLT reconstruction. The incomplete variables truncated conjugate gradient algorithm with an iterative permissible region shrinking strategy was employed as the optimization scheme to reconstruct source distributions. Simulation studies were conducted for single spherical sources with sizes from 0.5 to 3 mm radius at depth of 3–12 mm. The same configuration was also applied for the double source simulation with source separations varying from 3 to 9 mm. Experiments were performed in a standalone BLT/CBCT system. Two self-illuminated sources with 3 and 4.7 mm separations placed inside a tissue-mimicking phantom were chosen as the test cases. Live mice implanted with single-source at 6 and 9 mm depth, two sources at 3 and 5 mm separation at depth of 5 mm, or three sources in the abdomen were also used to illustrate the localization capability of the BLT system for multiple targets *in vivo*.

Results: For simulation study, approximate 1 mm accuracy can be achieved at localizing center of mass (CoM) for single-source and grouped CoM for double source cases. For the case of 1.5 mm radius source, a common tumor size used in preclinical study, their simulation shows that for all the source separations considered, except for the 3 mm separation at 9 and 12 mm depth, the two neighboring sources can be resolved at depths from 3 to 12 mm. Phantom experiments illustrated that 2D bioluminescence imaging failed to distinguish two sources, but BLT can provide 3D source localization with approximately 1 mm accuracy. The *in vivo* results are encouraging that 1 and 1.7 mm accuracy can be attained for the single-source case at 6 and 9 mm depth, respectively. For the 2 sources *in vivo* study, both sources can be distinguished at 3 and 5 mm separations, and approximately 1 mm localization accuracy can also be achieved.

Conclusions: This study demonstrated that their multispectral BLT/CBCT system could be potentially applied to localize and resolve multiple sources at wide range of source sizes, depths, and separations. The average accuracy of localizing CoM for single-source and grouped CoM for double sources is approximately 1 mm except deep-seated target. The information provided in this study can be instructive to devise treatment margins for BLT-guided irradiation. These results also suggest that the 3D BLT system could guide radiation for the situation with multiple targets, such as metastatic tumor models. © *2016 American Association of Physicists in Medicine.* [http://dx.doi.org/10.1118/1.4947481]

Key words: bioluminescence tomography, preclinical study, small animal irradiator, radiation therapy, image-guidance

1. INTRODUCTION

In preclinical radiation research, the advent of x-ray CT/cone-beam CT (CBCT) guided systems[1–6] has created new opportunities to test basic radiobiological hypotheses in ways that have not been feasible previously. Clarkson *et al.*[3] reported a CBCT based small animal image-guided irradiation system, X-Rad 225Cx, in which both the x-ray tube and the flat-panel detector are mounted on a rotational C-arm gantry. The group at Stanford University added radiotherapy functionality to a micro-CT scanner by utilizing a 2D translation stage to position the animal and a variable circular collimator.[7] In our laboratory, we designed and built a small animal radiation research platform (SARRP)[1,8] equipped with an on-board CBCT for focal irradiation guidance.

Although CT or CBCT is the major imaging modality to guide radiation in preclinical applications,[3,4,9–11] it remains challenging to localize soft tissue targets. Bioluminescence imaging (BLI) can serve as potential image guidance. Since genetically engineered mouse models (GEMMs) are widely used in oncologic and radiobiology research, BLI can be readily applied to an existing animal model with *luc* gene, which can express luciferase enzyme by adding luciferin. The luciferase, combined with the luciferin, oxygen, and ATP, can result in bioluminescence. While the labeled cells multiply, the *luc* gene also propagates with the cells. It eliminates the signal reduction due to cell division. This genetic reporter, bioluminescence, is expected to provide strong soft tissue contrast than CT/CBCT such as in brain, prostate, or abdomen region. The low cost, nonionizing radiation, and compact features also make BLI an attractive modality for image guidance. Due to the complex nonlinear relationship between signal strength, surface emittance, and tissue optical properties, we demonstrated that BLI alone is limited in its ability to provide accurate 3D target position.[12] However, with a sophisticated reconstruction algorithm and an appropriate mathematical model describing light transport in tissue, 3D bioluminescence tomography (BLT) based on the 2D BLI measured on the object surface can reveal the 3D distribution of internal bioluminescent sources.[12–19] Our group first proposed an integrated x-ray CBCT and 3D BLT system to guide SARRP irradiation.[12,20] Our preliminary study[12] demonstrated that in both phantom and mouse carcass, the BLT system can recover the center of mass (CoM) of a self-illuminated light source with an average accuracy of 1 mm.

At the time of writing this paper, there are 50 institutes worldwide with SARRP in place. The robotic-controlled gantry and animal stage enable noncoplanar delivery with high accuracy of 0.2 mm.[1] It also renders that the localization uncertainty of the SARRP-BLT system is strongly associated with the reconstruction. Due to the nature of the strong light scattering in tissue and the complexity of the tomography, it is known that the target localization accuracy of the BLT largely depends on the reconstruction algorithm and system configuration. A systematic study to assess the localization capability, specific for our system, will be a great interest for the SARRP users and the readers interested in applying BLT for radiation therapy. In this work, we extended our previous study[12] by systematically assessing the localization capability of our BLT system in simulation, phantom, and *in vivo* environments. In particular, we investigated the accuracy of BLT-derived CoM as a function of depth and target size for the single-source case in a simulated cylindrical phantom. We also demonstrated the localization accuracy in an *in vivo* environment. We further studied the resolving power of our BLT system for two neighboring sources in the simulated phantom and the accuracy of localizing CoM for different source separations, depth, and source sizes. The resolving power for multiple sources was also demonstrated in a tissue-simulating phantom and live mice.

2. MATERIALS AND METHODS

2.A. BLT reconstruction

Photon transport in tissue at the wavelengths of bioluminescence is dominated by scattering. The diffusion approximation (DA) is widely used to describe light propagation under these conditions.[21] In continuous wave mode, the DA and the Robin-type boundary condition can be written as

$$\begin{cases} -\nabla \cdot D(r)\nabla\Phi(r) + \mu_a(r)\Phi(r) = S(r),\ r \in \Omega \\ \Phi(\xi) + 2A\hat{n} \cdot D(\xi)\nabla\Phi(\xi) = 0,\ \xi \in \partial\Omega \end{cases}, \quad (1)$$

where $\Phi(r)$ is the photon fluence rate at location r in domain Ω, $D(r) = 1/(3(\mu_a + \mu_s'))$ is the diffusion coefficient, and μ_a and μ_s' are absorption and reduced scattering coefficients, respectively. $S(r)$ is the bioluminescence source distribution. ξ represents points on the imaging object boundary and A depends on the refractive index mismatch between tissue and

air. $\hat{n}$ is the unit vector pointed outward normal to the boundary $\partial\Omega$.

Equation (1) can be further expressed in the form of Green's function. The Green's function links the fluence rate at the object boundary and the bioluminescence source distribution. Multispectral BLT was employed in this study to improve localization accuracy.[14,16] The fluence rate $\varphi(\lambda_k)$, measured at the boundary at wavelength λ_k, linked to the bioluminescence source distribution s at 3D mesh nodes can be described as[22,23]

$$\begin{bmatrix} \varphi(\lambda_1) \\ \vdots \\ \varphi(\lambda_k) \end{bmatrix} = \begin{bmatrix} \eta(\lambda_1)G(\lambda_1) \\ \vdots \\ \eta(\lambda_k)G(\lambda_k) \end{bmatrix} [s]$$

or in simplified form

$$\varphi = \tilde{G}s, \tag{2}$$

where $G(\lambda_k)$ is the Green's function at wavelength λ_k, and $\eta(\lambda_k)$ is the relative spectrum weight which accounts for the source emission spectrum, the transmission of individual filters, and CCD quantum efficiency at different wavelengths. $\tilde{G}$ is the weighted Green's function $\eta(\lambda_k)G(\lambda_k)$. A modified version of the open source software NIRFAST (Refs. 24 and 25) was used to generate the Green's function using the finite element method (FEM) as well as to discretize the CBCT image of the object to generate the 3D mesh for the BLT reconstruction.

To avoid biasing the reconstruction algorithm by larger signals at longer wavelength (due to lower attenuation),[26] the measurements φ and the weighted Green's function $\tilde{G}$ at each wavelength were divided by the maximum value of the measurements. By minimizing the deviation between the computed and measured fluence rates at the object boundary, we can reconstruct the optimal bioluminescence source distribution s. We formulated the BLT reconstruction in the following minimization scheme with L_1-norm regularization, which is expected to appropriately retrieve sources sparely distributed,

$$\min_s \frac{1}{2}\left\|\bar{G}s - \bar{\varphi}\right\|_2^2 + \tau\|s\|_1, \tag{3}$$

where $\bar{G}$ and $\bar{\varphi}$ are the normalized Green's function and measured fluence rate at the boundary and $\bar{G}s$ is the corresponding computed fluence rate; $\|\cdot\|_2^2$ donates the square of the Euclidean norm, such as $\sum_i(\bar{G}s-\bar{\varphi})_i^2$, $\|s\|_1 = \sum_i |s_i|$ is the L_1-norm of s, and τ is a non-negative regularization parameter which controls the trade-off between the data-fitting part $\left\|\bar{G}s - \bar{\varphi}\right\|_2^2$ and the L_1-norm regularizer $\|s\|_1$. In this study, CCD counts per pixel area were chosen as the measurement quantity at the boundary and were not linked to absolute fluence rate. Further study to calibrate CCD counts to absolute fluence rate at the boundary is warranted.[20]

To solve Eq. (3) stably, we employed an iterative reconstruction framework by combining the incomplete variables truncated conjugate gradient (IVTCG) algorithm[27] with an iterative permissible region shrinking strategy.[26] Specifically, at the ith iteration, a solution $s^{(i)}$ of Eq. (3) was solved by the IVTCG algorithm and the objective function

$$f_i = \sum \left\|\bar{G}s^{(i)} - \bar{\varphi}\right\|_1 \tag{4}$$

was calculated. Depending on the solution, the permissible region shrank with iteration, starting from the mesh volume of the imaging object except surface nodes to a small volume containing the bioluminescence sources. The final BLT reconstruction source distribution was the solution corresponding to the minimum objective function, Eq. (4). Figure 1 shows the flow chart of the BLT reconstruction procedure.

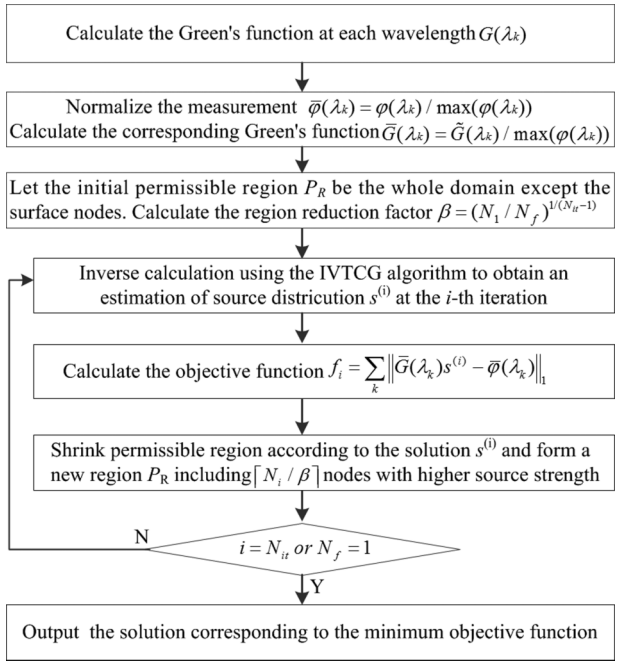

FIG. 1. Flow chart of the iterative BLT reconstruction procedure. In each iteration, the permissible region shrinks by sorting the resolved source strength at each node in descending order, and then selecting $\lceil N_i/\beta \rceil$ nodes with higher source strength, where N_i is the total number of nodes in the permissible region at the ith iteration and $\lceil N_i/\beta \rceil$ is the nearest integer greater than or equal to N_i/β. The initial permissible region is the whole domain except the surface nodes and contains N_1 nodes. Throughout the iterative process, the number of nodes in the permissible region shrinks from N_1 to N_f (final number of nodes). In our implementation, N_f and N_{it} (number of iterations) were set to 1 and 20, respectively.

2.B. Simulation

A series of tests were conducted based on a simulated cylindrical phantom, 18 mm radius and 24 mm height. Single or two neighboring simulated spherical sources were embedded in the cylindrical phantom. For the forward calculation in the simulation, the DA [Eq. (1)] and FEM were chosen to calculate the fluence rate at the phantom surface produced by the bioluminescence sources. The cylindrical phantom was discretized into a tetrahedral mesh with denser nodes in the source region, to provide accurate fluence rate calculated at the phantom surface. Depending on the specific source configuration, the forward mesh is allowed to be different between cases. To mimic measurement uncertainty,

3% Gaussian white noise was added to the simulated boundary data. For reconstruction, a uniform tetrahedral mesh, approximately 10 000 nodes and 53 000 elements generated from COMSOL 4.5 (COMSOL, Inc., Burlington, MA, USA), was used for all the cases in Sec. 2.B without any *a priori* information about source size and position. The iterative algorithm described in Sec. 2.A was used to reconstruct the source distributions. Because the amplitude of the simulated noise was randomly determined, for each simulated experiment, five independent runs were performed. The reconstruction accuracy was assessed by CoM deviation, i.e., the localization error between the reconstructed CoM and the actual source center. To simulate the measurement conditions of our BLT system,[12,20] single-projection data (at 1 mm spacing, total 4020 number of data points for 4 wavelengths) collected at the top surface perpendicular to the cylinder axis of the phantom were used for reconstruction. The refractive index 1.4 and optical properties shown in Table I were used for reconstruction. A regularization parameter, $\tau = 1 \times 10^{-7}$, determined empirically was applied for all the simulations.

2.B.1. Simulation 1: Single-source

Single-source simulations were designed to investigate the localization accuracy of the BLT system for targets with various sizes at different depths. The simulated sources were spherical in shape with radius of 0.5, 1.5, or 3 mm. Due to the phantom dimension, we considered 4 depths (from the top surface of the cylindrical phantom to the source center) in the following simulations. For sources with radius of 0.5 and 1.5 mm, depths of 3, 6, 9, and 12 mm were tested. To avoid a source boundary at the phantom surface, for the sources with 3 mm radius, depths of 4, 6, 9, and 12 mm were tested. There were a total of 12 testing cases for the single-source simulations. The forward meshes for these 12 cases varied slightly, containing about 11 000 nodes and 60 000 elements.

2.B.2. Simulation 2: Double sources

To investigate the resolving power of our BLT system, two identical spherical sources with equal intensity were placed in the cylindrical phantom at the same depth. The size and depth settings were the same as that of single-source cases. The edge-to-edge separations between the two sources were 3, 6 and 9 mm. A total of 36 testing cases were considered in the double sources simulations. Similar to the single-source simulation, the forward meshes varied in size according to the specific source settings, including around 11 000 nodes and 62 000 elements. In preclinical application, two neighboring sources in close vicinity are most likely regarded as a single target for irradiation. The grouped CoM which represents the CoM of the two sources was also calculated to assess the overall BLT localization accuracy.

TABLE I. Optical properties for simulation, phantom, and *in vivo* experiments.

	Wavelength	590 nm	610 nm	630 nm	650 nm
Simulation[a]	μ_a (mm^{-1})	0.1283	0.0396	0.0214	0.0156
	μ_s' (mm^{-1})	1.35	1.29	1.24	1.19
Phantom[b]	μ_a (mm^{-1})	0.0138	0.0094	0.0081	0.0077
	μ_s' (mm^{-1})	0.816	0.756	0.733	0.725
In vivo[c]	μ_a (mm^{-1})	0.0431	0.0127	0.0069	0.005
	μ_s' (mm^{-1})	1.53	1.46	1.40	1.35

[a]The μ_a and μ_s' for bowel tissue were chosen from Ref. 29.
[b]The optical properties of the phantom were measured independently, as described in Ref. 28.
[c]The μ_a for adipose tissue was chosen from Ref. 29. The μ_s' for soft tissues was calculated from Eq. (1) and Table II in Ref. 30.

2.C. Integrated CBCT/BLT system

The phantom and *in vivo* experiments were performed with a previously described BLT/CBCT system.[20] For CBCT imaging, the animal stage was rotated between a fixed horizontal x-ray source (Thermo Fisher Scientific, Waltham, MA, USA) and a CMOS detector panel (PerkinElmer, Waltham, MA, USA). The detector panel is 15×12 cm^2 with 75 μm pixel size. The standard settings for CBCT imaging were 65 kVp and 0.45 mA with spot size of 41 μm. For BLT, a 3-mirror system, filter wheel, and CCD camera (iKon-L 936, Andor Technology, Belfast, UK) mounted with a 35 mm f/1.4 lens (Rokinon, New York, NY, USA) were aligned perpendicular to the x-ray imaging axis. The BLI from the imaging object was directed to the CCD camera via the 3-mirror system. The CCD camera has high quantum efficiency (>90%) over the spectral range from 500 to 700 nm which is of interest for BLI. The camera was operated at −80 °C to reduce the dark current and thermal noise during image acquisition. To acquire multispectral BLIs, a computer controlled filter wheel was mounted in front of the lens, containing four 10 nm FWHM band-pass filters (50 mm diameter, Andover Corporation, Salem, NH, USA) spaced every 20 nm from 590 to 650 nm. The detail of our system calibration method can be found in Refs. 12 and 20.

Single projection of the BLI, top view of the object, was acquired for each wavelength. The optical background was subtracted for each BLI, followed by image uniformity correction. The BLIs were acquired at 0.6 mm/pixel (4×4 binning). For experiments with low light signal (*in vivo* single source at 9 mm depth), the images were acquired with 8×8 binning and interpolated to 4×4 binning for our software utility. Because the 610 nm image showed the strongest overall signal compared to the others, the positions of the surface data points were selected based on the 610 nm image, where the points with the intensities larger than 10% of the maximum value were chosen. The data points at the same surface location as that of the 610 nm data were also selected for the BLIs at other wavelengths. There were approximately a total of 1100–1300 and 2000–2600 surface data points for all four wavelengths for phantom and *in vivo* experiments, respectively. Because the surface points were selected based on the threshold, few *in vivo* cases, such as the three sources experiment, there were 1300 points. The selected surface BLI points were mapped onto the mesh surface generated from the

CBCT, according to the geometry calibration, which registers the 2D BLI and CBCT coordinates. These points were used for the reconstruction procedures described in Sec. 2.A.

2.D. Phantom experiments

A tissue-mimicking half-cylindrical phantom (15 mm radius × 41 mm height) with wavelength-dependent optical properties was employed.[12,20,28] Two sources, each consisting of four small cylindrical self-illuminated light sources (0.9 mm diameter × 2 mm length, Trigalight, mb-microtec ag, Niederwangen, Switzerland), were placed in the holes inside the phantom, which mimicked a small spherical source, approximately 1.5 mm in radius. Two cases were investigated: for the first case, the two sources were placed with an edge-to-edge separation of 4.7 mm. Multispectral images at 590, 610, 630, and 650 nm were acquired in 10 s exposure time per wavelength with 4×4 binning of the CCD pixels. For the second case, the two sources were separated by 3.0 mm. Multispectral images were acquired in 30 s exposure time per wavelength with 4×4 binning. The phantom CBCT image was cropped and discretized into a 3D tetrahedral mesh (approximately 12 000 nodes and 63 000 elements for case 1 and 11 000 nodes and 56 000 elements for case 2) for BLT reconstruction. To account for the positioning uncertainty of the mesh node generated from the NIRFAST module, three independent reconstructions based on three meshes were performed for each case. The refractive index value of 1.56 and optical properties, shown in Table I, were chosen for the reconstruction. The regularization parameter was set to $\tau = 1\times10^{-6}$ for the phantom experiments.

2.E. *In vivo* experiments

The *in vivo* experiments were carried out in accordance with the Johns Hopkins Animal Care and Use Committee. Three experiments were performed to assess the *in vivo* localization capability of the BLT system for multiple sources at different depths and separations. For the first case, single cylindrical Trigalight source (0.9 mm diameter × 2 mm length) was surgically implanted in a mouse abdomen at 6 and 9 mm depth. In order to control the depth, the source was tied on a suture (Nylon 7/0, AROSurgical Instruments, Inc., Newport Beach, CA, USA). The ends of the suture were kept outside of the mouse body to adjust the source position. The regularization parameters $\tau = 1\times10^{-6}$ and 1×10^{-5} were chosen for the 6 and 9 mm study, respectively. For the second case, we studied the resolving power of the BLT system *in vivo* by implanting two Trigalight sources at edge-to-edge separation of 3 and 5 mm at 5 mm depth in mouse abdomen. To control the source separation, two sources were, respectively, placed into two glass tubes (1.5 mm diameter × 15 mm length) and the tubes were glued on a spacer with desired separation. The regularization parameters $\tau = 1\times10^{-5}$ and 5×10^{-5} were chosen for 3 and 5 mm cases, respectively. Three mice were used for the first and second experiments. For the third case, three sources were surgically implanted in the mouse abdomen to illustrate the application of BLT system for multiple targets. The regularization parameter for the third case was set to $\tau = 1\times10^{-6}$.

The mouse was anesthetized with 1%–2% isoflurane in oxygen during the surgical and imaging procedures. Before the BLT experiment, to remove hair, the mouse was shaved and chemically depilated (Nair, Church & Dwight Co., NJ, USA). The mouse was placed at the supine position, and the abdomen was prepared with Betadine solution (10% topical solution). At 1 cm above the abdominal wall, a transverse incision was made and the peritoneal cavity was opened. The light sources were placed inside the abdomen. The abdomen was closed, and the peritoneum and muscle were sutured with Nylon 7/0 and the skin with Nylon 6/0. The mouse was then placed on the animal stage inside the imaging chamber. Multispectral BLIs at 590, 610, 630, and 650 nm were acquired in between 30 and 300 s exposure time per wavelength with 4×4 or 8×8 binning, depending on the source depth.

A section of the torso was cropped from the CBCT image to generate a 3D tetrahedral mesh (10 000–18 000 nodes and 60 000–90 000 elements depending on the mouse size) for the reconstruction. The 3D source distribution was reconstructed using a refractive index value of 1.4. The same optical properties presented in our previous publication[12] were chosen for the *in vivo* study and are listed in Table I. Since the sources were implanted in the abdomen, we assumed homogeneous but wavelength-dependent optical properties for the BLT reconstruction. As described in Sec. 2.D, three independent reconstructions based on three meshes were also performed for each *in vivo* study.

3. RESULTS

3.A. Simulation

Figure 2 shows the CoM deviation for different source sizes at depths from 3 to 12 mm. The mean CoM deviation for all

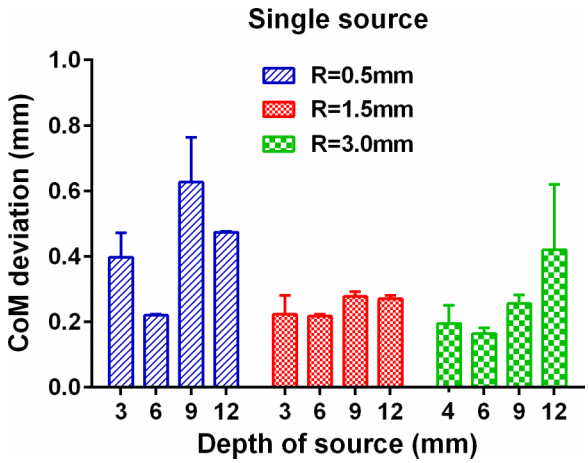

FIG. 2. The CoM deviation (mean with standard deviation) for source sizes 0.5, 1.5, and 3 mm in radius vs depth for the single-source simulation. Twelve scenarios were considered: single-source with radius of 0.5 and 1.5 mm at depth of 3, 6, 9, and 12 mm; single-source with radius of 3 mm at depth of 4, 6, 9, and 12 mm.

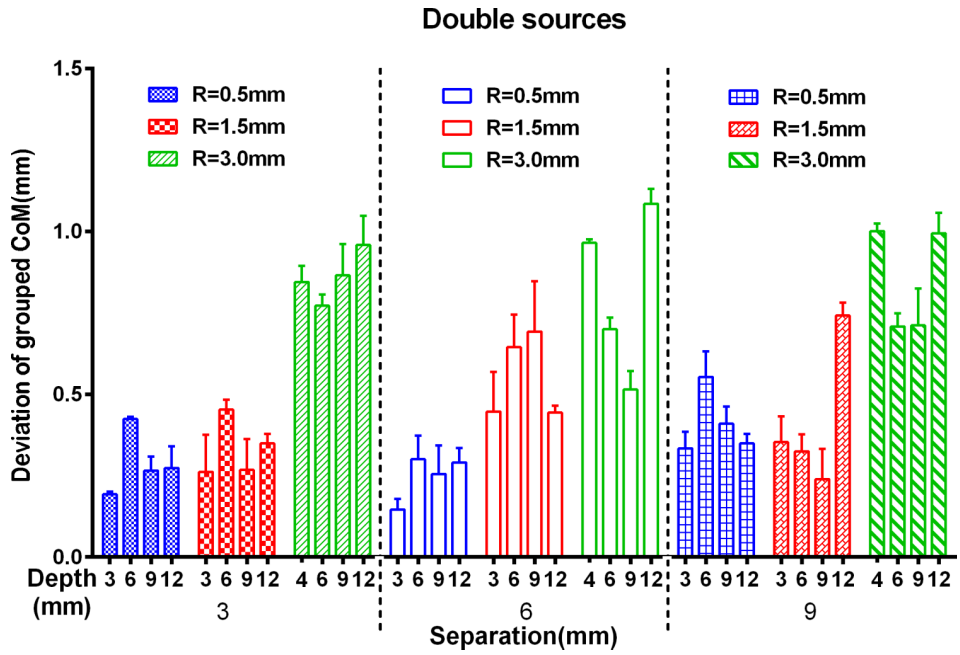

FIG. 3. Deviation of grouped CoM (mean with standard deviation) as function of depth, source separation, and size. Thirty-six scenarios were considered: spherical sources of 0.5 and 1.5 mm radius at depth of 3, 6, 9, and 12 mm; sources of 3 mm radius at depth of 4, 6, 9, and 12 mm. The separations are 3, 6, and 9 mm.

the depths considered is 0.5, 0.2, and 0.3 mm for the 0.5, 1.5, and 3 mm radius sources, respectively.

For the cases of double sources, Fig. 3 shows the grouped CoM deviation as a function of depth, source separation, and size. CoM localization accuracy within 1 mm is achieved in all but one of the cases. The exception is the 3 mm radius sources with separation of 6 mm at 12 mm depth (1.1 mm). The average grouped CoM errors for source sizes of 0.5, 1.5,

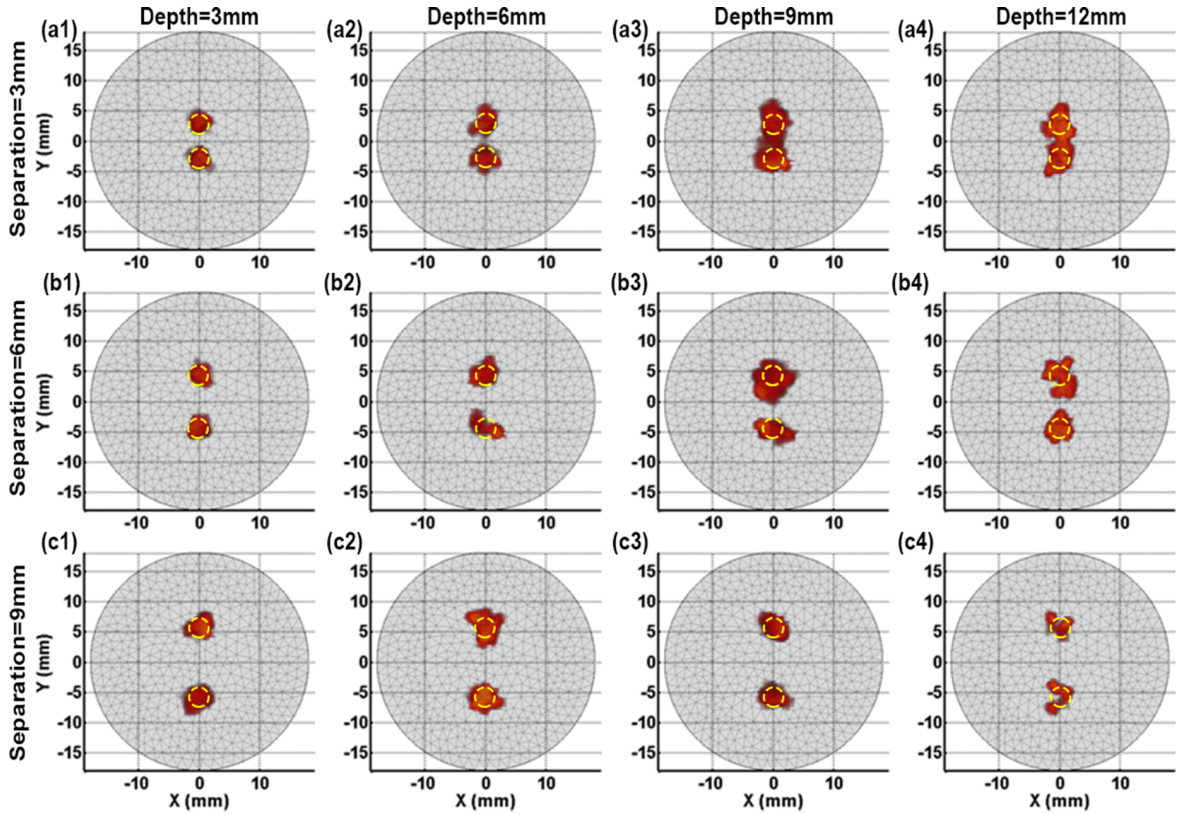

FIG. 4. Reconstruction results of double sources (1.5 mm radius) at different depths and separations. (a1)–(a4) show the top views (X–Y plane) for the 3 mm separation at depth of 3, 6, 9, and 12 mm, respectively. (b1)–(b4) and (c1)–(c4) show the corresponding results for the 6 and 9 mm separation, respectively. The yellow circles outline the true source. Voxels with reconstructed value greater than 10% of the maximum are shown.

and 3 mm radius are 0.3 ± 0.1, 0.4 ± 0.2, and 0.8 ± 0.2 mm, respectively, for all the depths and separations considered.

Figure 4 illustrates the resolution of two closely spaced sources. We show the case of the 1.5 mm radius source because this size of tumor is commonly used in preclinical studies. Our simulation shows that for almost all the source separations considered, the two 1.5 mm radius sources can be resolved at depths from 3 to 12 mm while maintaining a localization accuracy of the grouped CoM to within 1 mm. Figures 4(a3) and 4(a4) show the challenging scenarios, 3 mm separation at depth 9 and 12 mm, where the sources are not clearly resolved. Excluding these cases, the average positioning error of the reconstructed CoM for the individual source is at 0.5 ± 0.3 mm.

3.B. Phantom experiment

Due to the phantom geometry and source locations, the two sources are not resolved in 2D BLI [Figs. 5(a) and 5(d)]. For the first case, two sources with 4.7 mm separation were placed inside the half-cylinder phantom at depth of 6.8 mm for source 1 (s1) and 5.0 mm for source 2 (s2). Since s1 was placed at deeper depth, a larger CoM offset is observed in the Z-axis (depth direction). The average 3D CoM deviations of s1 and s2 are 1.4 and 0.6 mm. The deviation of the grouped CoM acquired from the BLT and CBCT is 1.2 mm. Figure 5(d) illustrates the overlay of BLI with the CBCT slice for the second case where two sources were placed inside the phantom with separation of 3.0 mm at depth 6.8 mm. The deviation of the grouped CoM acquired from the BLT and CBCT is 1.1 mm. The mean 3D CoM offsets of the two individual sources is at 1 mm.

3.C. *In vivo* experiment

The representative results of the *in vivo* single-source study are shown in Fig. 6. For the 6 mm case, the average CoM

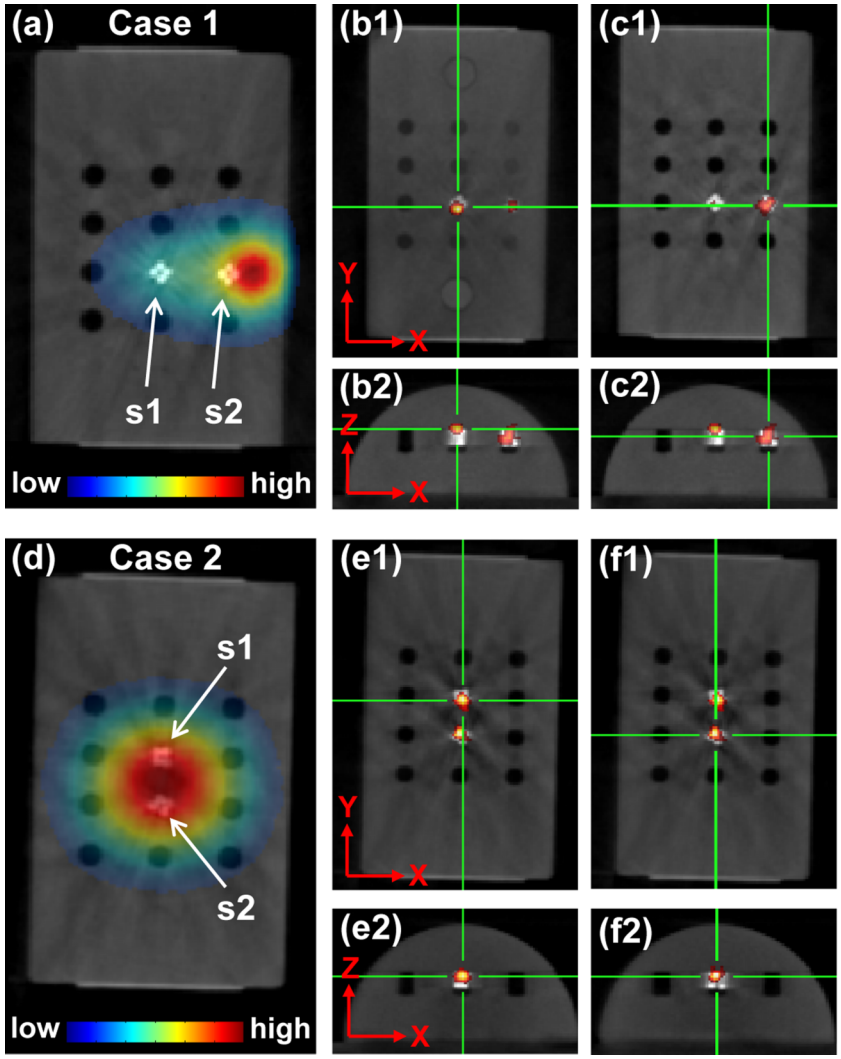

FIG. 5. Phantom experiments. Case 1: source 1 (s1) and source 2 (s2) were placed 4.7 mm apart at depth of 6.8 mm for s1 and 5.0 mm for s2. The white dots shown in the figures are the true sources, and the red dots are the BLT reconstructed sources. (a) is the top view of BLI (at 610 nm) overlapped with CBCT slice. (b1) and (b2) are the coronal and transverse views of BLT overlapped with CBCT for the s1. (c1) and (c2) are the corresponding views for the s2. Case 2: s1 and s2 were placed 3 mm apart at equal depth 6.8 mm. (d) is the top view of BLI (at 610 nm) overlapped with CBCT slice. (e1) and (e2) are the coronal and transverse views of BLT overlapped with CBCT for s1 and (f1) and (f2) are the corresponding images for s2. The cross is centered at the CoM of the reconstructed sources. Voxels with reconstructed value greater than 10% of the maximum are shown. (See color online version.)

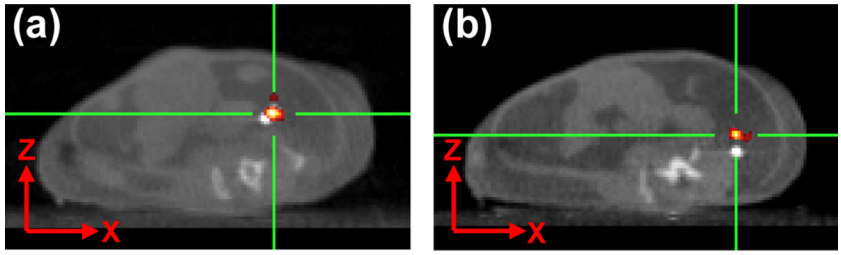

FIG. 6. The mouse was implanted with single-source at depth 6 (a) and 9 (b) mm, in the abdomen. The white dots shown in the figures are the true sources, and the red dots are the BLT reconstructed sources. Voxels with reconstructed value greater than 10% of the maximum are shown. (See color online version.)

deviation between the true and BLT reconstructed sources is 1.0 ± 0.3 mm. For the 9 mm study, the major offset is in the depth direction [Fig. 6(b)] and the average CoM offset is 1.7 ± 0.1 mm. It suggests that multiprojection and organ-specific optical properties are likely needed for deep-seated tumor in an *in vivo* environment.

The representative results of the two sources are shown in Fig. 7. The 2D BLI overlaid on the CBCT images is shown in Figs. 7(a1) and 7(b1) for the cases of 5 and 3 mm separation, respectively. Again, 2D BLI failed to distinguish two neighboring sources, but 3D BLT can reveal the sources nicely [Figs. 7(a1) vs 7(a2)–7(a4) and 7(b1) vs 7(b2)–7(b4)]. More interestingly, the two sources are equal strength but the BLI image [Fig. 7(a1)] incorrectly suggests the sources at different strength. The average deviation of the grouped CoM acquired from the BLT and CBCT is 1.0 ± 0.2 and 0.7 ± 0.4 mm for the 5 and 3 mm study, respectively. The separation between the two reconstructed BLT sources differs than the true separation by 0.02 and 0.66 mm for the 5 and 3 mm cases. It is worthwhile to mention that the 3 mm separation is the most challenging case and depending on the choice of the mesh resolution, it can possibly lead two close sources barely distinguished. For the individual sources, we can reach approximately 1 mm accuracy of the BLT reconstructed CoM for both cases [Figs. 7(a3), 7(a4), 7(b3), and 7(b4)].

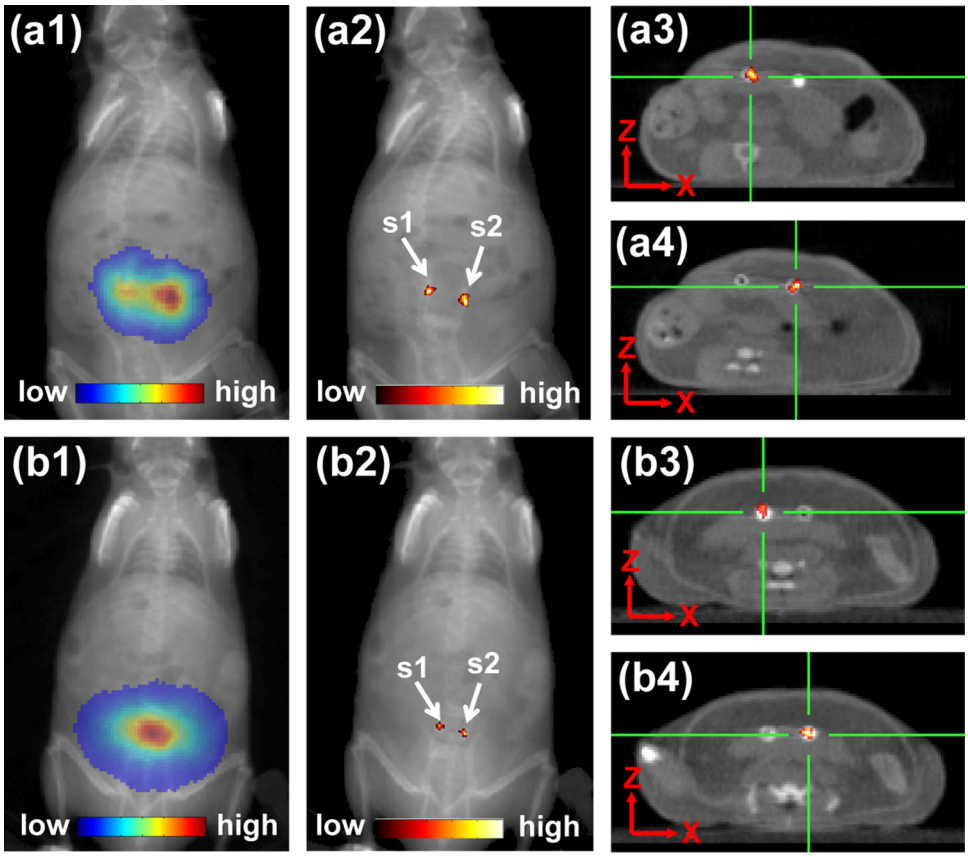

FIG. 7. The mouse was implanted with two sources (s1 and s2) at separation 5 [(a1)–(a4)] and 3 [(b1)–(b4)] mm at depth of 5 mm, in the abdomen. The white dots shown in the figures are the true sources, and the red dots are the BLT reconstructed sources. (a1) The anterior–posterior view of BLI (at 610 nm) overlaid with CBCT. (a2) The BLT reconstructed sources overlaid with CBCT. [(a3) and (a4)] The transverse views of BLT overlaid with CBCT. The cross is centered at the CoM of the reconstructed sources. (b1)–(b4) are the corresponding plots for the case of 3 mm separation. Voxels with reconstructed value greater than 10% of the maximum are shown. (See color online version.)

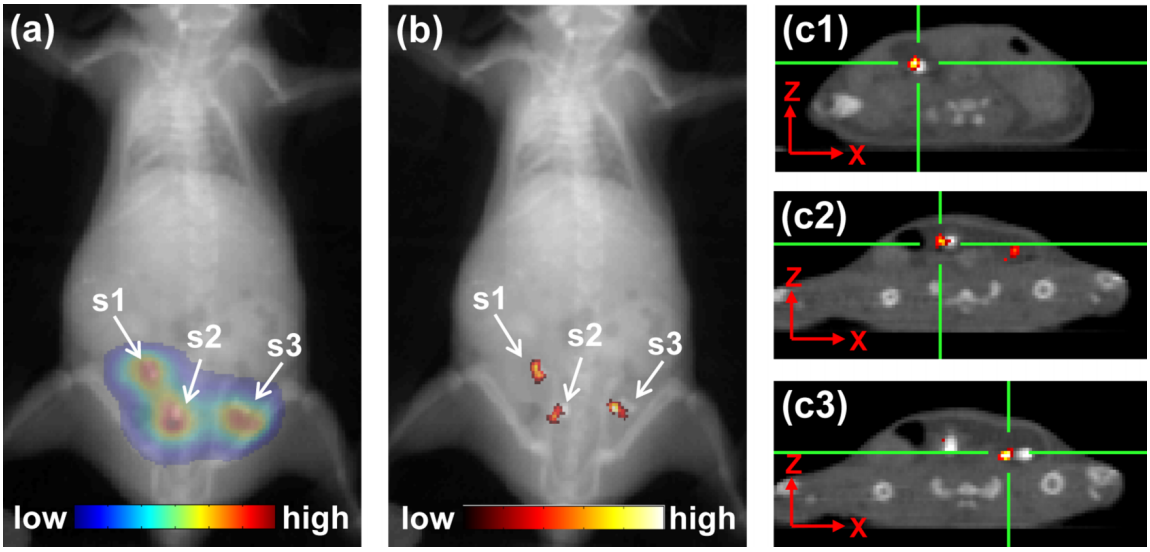

FIG. 8. The mouse was implanted with three light sources in the abdomen. The white dots shown in the figures are the true source location. (a) The anterior–posterior view of BLI (at 610 nm) overlaid with CBCT. (b) The BLT reconstructed sources overlaid with CBCT. [(c1)–(c3)] The transverse views of BLT overlaid with CBCT of source 1, 2, and 3, respectively. The cross is centered at CoM of the reconstructed sources. Voxels with reconstructed value greater than 10% of the maximum are shown.

The results with three sources are shown in Fig. 8. The 2D BLI and 3D BLT overlaid on the CBCT images are shown in Figs. 8(a) and 8(b), respectively. The transverse views of the BLT for each source are shown in Figs. 8(c1)–8(c3). The depth of the three sources is 3.3–3.5 mm. The distance between s1 and s2 is 5.5 and 6.9 mm between s2 and s3. The average CoM deviation for s1, s2, and s3 is 0.5 ± 0.1, 1.2 ± 0.1, and 1.3 ± 0.0 mm, respectively. The average grouped CoM of the three sources is 0.5 ± 0.1 mm.

4. DISCUSSION

In preclinical radiation application, x-ray CT/CBCT is limited in guiding irradiation for soft tissue targets. As a complementary method, our initial study[12] showed that the BLT SARRP system can locate the CoM of small cylindrical targets in 3D with 1 mm accuracy for both phantom and mouse carcass environments. Since small animal irradiators were commercialized 5 years ago, close to 75 systems, 50 of them SARRPs, have been deployed in laboratories worldwide. It is well known that reconstruction accuracy of the BLT highly depends on the algorithm and system configuration. A systematic study to assess the target localization capability particular for our system will be a great interest for the SARRP users. This work is the very few (if any) studies providing an extensive set of objective performance evaluations for double sources in simulations, phantoms, and *in vivo* environment. This study is informative for assessing the localization uncertainty of the BLT-guided system and for preclinical application of multiple soft tissue targets, such as metastatic tumor model. This is important when radiation is currently being tested as a modality beyond that of local control, particularly in combination with immunotherapy.

Several investigators[15,31–33] have proposed to utilize CT/CBCT to provide anatomical information and surface contour for BLT reconstruction. Although the previously published systems[15,31–33] have few features similar to ours, our BLT system is unique that all the following aspects were integrated. First, animal is placed in a nature position (supine or prone) rather than the upright position, which avoids discomfort and organ sagging. This setting largely eases the animal set up, critical for the radiobiological studies commonly requiring high throughput. Second, although single projection is utilized in this study, the 3-mirror system can rotate around the animal in supine/prone position to capture the bioluminescence light at different rotation angles and form a multiple projection BLT. Third, filters are utilized for multispectral acquisition to increase reconstruction accuracy. Last, CBCT and BLT shared a common animal stage. The two systems are fully integrated by geometry registration. Animal transport between the two systems is eliminated.

We recently[34,35] showed that based on 2D BLI, a vertical beam directed at the highest bioluminescence intensity on the animal surface deviates from the CoM of an internal source by more than 3 mm. Including other sources of setup uncertainty,[36] an undesirably large beam aperture greater than 18 mm in diameter, more than half of the width of the mouse abdomen, would be required to ensure coverage of a small 1.5 mm radius tumor. Figures 2 and 6 show that for the single-source case, depending on the depth, the localization error of the single projection BLT can be at 1 mm accuracy. A significantly smaller collimator, in 8 mm diameter, can be chosen to irradiate the target and avoid unwanted dose to nearby organs at risk. Although our *in vivo* results show larger CoM deviation at deeper depth 9 mm, the 1.7 mm deviation is still superior to the 2D BLI estimation. The localization uncertainty for deep-seated target is likely improved by the

multiple projections BLT (Ref. 37) and organ-specific optical properties.

Virostko *et al.*[38] characterized the commercially available BLT system (IVIS 200, Xenogen, Alameda, CA, US) by investigating the effect of source depth on the accuracy of reconstructed source location and ability to distinguish two separated luminescent beads. The single view approach and the assumption of homogeneous optical properties were applied in their work. The authors concluded that for the IVIS 200 system, two adjacent sources cannot be resolved unless they are separated by twice their depth. We adopted a similar approach but expanded the testing cases to different source sizes using a simulated phantom. Although the simulation can never replace the *in vivo* experiments, the simulations provide an idea of the best performance that could be possibly achieved *in vivo* and allow us to test many situations which is not feasible in the *in vivo* setting. For sources of 1.5 and 3 mm radius, our BLT reconstruction algorithm is not confined by the limitation described by Virostko *et al.*[38] and is able to resolve the two adjacent sources with 3 mm separation from 3 to 4 mm depth and with 6 and 9 mm separation up to 12 mm depth. Figure 7 further demonstrates the capability of our BLT system, in an *in vivo* environment, to distinguish the two small sources as close as 3 mm at the depth of 5 mm. In practice, two sources in close proximity are likely regarded as a single target for the purposes of irradiation. However, a larger margin would appear to be required following the 2D bioluminescence distribution. In contrast, 3D BLT can effectively provide accurate guidance for irradiation margins. Our simulation, phantom, and *in vivo* results showed that overall 1 mm accuracy for the grouped CoM can be achieved for all the cases. Because of the scale of small animal models, tight and precise margins are important to reduce the dose to organs at risk, which can confound the experimental outcome.

To achieve comprehensive BLT-guided radiation therapy and devise accurate margins, we recognize that target shape reconstruction can be equally important as CoM localization. The results show that our BLT algorithm can approximately delineate spherical source distributions (Fig. 4). In a real life specimen, the target distributions can be more complicated than the source configurations chosen in this study. A more accurate light transport model, the SP_3 approximation, may provide 3D target shape in greater detail.[18] With the capability to reveal multiple targets and their distribution, the multispectral BLT-SARRP system will be able to facilitate the use of complex delivery strategies,[1,39,40] particularly useful for targeting orthotopic tumors.

Although our phantom and *in vivo* results (Figs. 5–8) show the grouped CoM of the multiple targets and the CoM of the individual source can be reconstructed with 1 mm accuracy, larger CoM deviations were observed for few cases. This may be caused by the single projection approach and differences in optical properties in the source-implanted region from those we used for reconstruction. The single view data may explain why our CoM offset was most noticeable in the depth direction and this can likely be reduced with more views at the cost of longer data acquisition. Homogenous optical properties were assumed in this study and this is a common assumption in commercial BLT systems.[19,38] We do not discount the importance of applying heterogeneous optical properties. The use of diffuse optical tomography[41] or organ-dependent optical properties is expected to provide a more accurate description of light transportation in the heterogeneous mouse. In addition, the IVTCG algorithm is a regularization-based method. The reconstruction result inevitably depends on the choice of the regularization parameter. In this work, the regularization parameter is empirically determined. One would recognize that searching the optimal regularization parameter for an ill-posed problem is not a trivial task and an adaptive method[42] can potentially improve this aspect.

5. CONCLUSION

A systematic study was conducted, in simulation, phantom, and *in vivo* environments, to assess the multispectral BLT system in localizing and resolving multiple sources at different source sizes, depths, and separations. The average accuracy of localizing the CoM for a single-source and grouped CoM for multiple targets is 1 mm except deep-seated targets. The information provided in this study can be useful in deciding treatment margins for the BLT-guided system. These results also suggest that the 3D BLT system can be potentially applied to guide radiation for multiple soft tissue targets.

ACKNOWLEDGMENTS

The authors would like to thank Dr. Phuoc T. Tran, Katriana Nugent, and Matthew Ballew for providing the animals for study. This work is supported by NIH Grant No. R01 CA 158100 and Xstrahl Ltd., and Dr. Jingjing Yu is also supported by China NNSFC Grant Nos. 61401264 and 61372046. Dr. John W. Wong and Dr. Iulian I. Iordachita receive royalty payment from a licensing agreement between Xstrahl Ltd. and Johns Hopkins University.

[a]J. Yu and B. Zhang contributed equally to this work.
[b]Author to whom correspondence should be addressed. Electronic mail: kwang27@jhmi.edu; Telephone: 614-282-0859; Fax: 410-502-1419.

[1]J. Wong, E. Armour, P. Kazanzides, I. Iordachita, E. Tryggestad, H. Deng, M. Matinfar, C. Kennedy, Z. Liu, T. Chan, O. Gray, F. Verhaegen, T. McNutt, E. Ford, and T. L. DeWeese, "High-resolution, small animal radiation research platform with x-ray tomographic guidance capabilities," Int. J. Radiat. Oncol., Biol., Phys. **71**, 1591–1599 (2008).
[2]E. Tryggestad, M. Armour, I. Iordachita, F. Verhaegen, and J. W. Wong, "A comprehensive system for dosimetric commissioning and Monte Carlo validation for the small animal radiation research platform," Phys. Med. Biol. **54**, 5341–5357 (2009).
[3]R. Clarkson, P. E. Lindsay, S. Ansell, G. Wilson, S. Jelveh, R. P. Hill, and D. A. Jaffray, "Characterization of image quality and image-guidance performance of a preclinical microirradiator," Med. Phys. **38**, 845–856 (2011).
[4]S. Stojadinovic, D. A. Low, A. J. Hope, M. Vicic, J. O. Deasy, J. Cui, D. Khullar, P. J. Parikh, K. T. Malinowski, E. W. Izaguirre, S. Mutic, and P. W. Grigsby, "MicroRT-small animal conformal irradiator," Med. Phys. **34**, 4706–4716 (2007).
[5]E. E. Graves, H. Zhou, R. Chatterjee, P. J. Keall, S. S. Gambhir, C. H. Contag, and A. L. Boyer, "Design and evaluation of a variable aperture collimator for conformal radiotherapy of small animals using a microCT scanner," Med. Phys. **34**, 4359–4367 (2007).

[6]R. Pidikiti, S. Stojadinovic, M. Speiser, K. H. Song, F. Hager, D. Saha, and T. D. Solberg, "Dosimetric characterization of an image-guided stereotactic small animal irradiator," Phys. Med. Biol. **56**, 2585–2599 (2011).
[7]H. Zhou, M. Rodriguez, F. van den Haak, G. Nelson, R. Jogani, J. Xu, X. Zhu, Y. Xian, P. T. Tran, D. W. Felsher, P. J. Keall, and E. E. Graves, "Development of a micro-computed tomography-based image-guided conformal radiotherapy system for small animals," Int. J. Radiat. Oncol., Biol., Phys. **78**, 297–305 (2010).
[8]M. Matinfar, E. Ford, I. Iordachita, J. Wong, and P. Kazanzides, "Image-guided small animal radiation research platform: Calibration of treatment beam alignment," Phys. Med. Biol. **54**, 891–905 (2009).
[9]B. C. Baumann, J. L. Benci, P. P. Santoiemma, S. Chandrasekaran, A. B. Hollander, G. D. Kao, and J. F. Dorsey, "An integrated method for reproducible and accurate image-guided stereotactic cranial irradiation of brain tumors using the small animal radiation research platform," Transl. Oncol. **5**, 230–237 (2012).
[10]E. C. Ford, P. Achanta, D. Purger, M. Armour, J. Reyes, J. Fong, L. Kleinberg, K. Redmond, J. Wong, M. H. Jang, H. Jun, H. J. Song, and A. Quinones-Hinojosa, "Localized CT-guided irradiation inhibits neurogenesis in specific regions of the adult mouse brain," Radiat. Res. **175**, 774–783 (2011).
[11]K. J. Redmond, P. Achanta, S. A. Grossman, M. Armour, J. Reyes, L. Kleinberg, E. Tryggestad, A. Quinones-Hinojosa, and E. C. Ford, "A radiotherapy technique to limit dose to neural progenitor cell niches without compromising tumor coverage," J. Neuro-Oncol. **104**, 579–587 (2011).
[12]B. Zhang, K. K. Wang, J. Yu, S. Eslami, I. Iordachita, J. Reyes, R. Malek, P. T. Tran, M. S. Patterson, and J. W. Wong, "Bioluminescence tomography guided radiation therapy for preclinical research," Int. J. Radiat. Oncol., Biol., Phys. **94**, 1144–1153 (2016).
[13]X. Gu, Q. Zhang, L. Larcom, and H. Jiang, "Three-dimensional bioluminescence tomography with model-based reconstruction," Opt. Express **12**, 3996–4000 (2004).
[14]H. Dehghani, S. C. Davis, S. Jiang, B. W. Pogue, K. D. Paulsen, and M. S. Patterson, "Spectrally resolved bioluminescence optical tomography," Opt. Lett. **31**, 365–367 (2006).
[15]W. Cong, G. Wang, D. Kumar, Y. Liu, M. Jiang, L. Wang, E. Hoffman, G. McLennan, P. McCray, J. Zabner, and A. Cong, "Practical reconstruction method for bioluminescence tomography," Opt. Express **13**, 6756–6771 (2005).
[16]C. Kuo, O. Coquoz, T. L. Troy, H. Xu, and B. W. Rice, "Three-dimensional reconstruction of *in vivo* bioluminescent sources based on multispectral imaging," J. Biomed. Opt. **12**, 024007 (2007).
[17]Y. Lu, X. Zhang, A. Douraghy, D. Stout, J. Tian, T. F. Chan, and A. F. Chatzioannou, "Source reconstruction for spectrally-resolved bioluminescence tomography with sparse a priori information," Opt. Express **17**, 8062–8080 (2009).
[18]A. D. Klose, B. J. Beattie, H. Dehghani, L. Vider, C. Le, V. Ponomarev, and R. Blasberg, "*In vivo* bioluminescence tomography with a blocking-off finite-difference SP3 method and MRI/CT coregistration," Med. Phys. **37**, 329–338 (2010).
[19]A. Behrooz, C. Kuo, H. Xu, and B. Rice, "Adaptive row-action inverse solver for fast noise-robust three-dimensional reconstructions in bioluminescence tomography: Theory and dual-modality optical/computed tomography *in vivo* studies," J. Biomed. Opt. **18**, 76010 (2013).
[20]Y. Yang, K. K. Wang, S. Eslami, I. I. Iordachita, M. S. Patterson, and J. W. Wong, "Systematic calibration of an integrated x-ray and optical tomography system for preclinical radiation research," Med. Phys. **42**, 1710–1720 (2015).
[21]S. R. Arridge, "Optical tomography in medical imaging," Inverse Probl. **15**, R41–R93 (1999).
[22]W. Cong, K. Durairaj, L. V. Wang, and G. Wang, "A born-type approximation method for bioluminescence tomography," Med. Phys. **33**, 679–686 (2006).
[23]M. A. Naser and M. S. Patterson, "Algorithms for bioluminescence tomography incorporating anatomical information and reconstruction of tissue optical properties," Biomed. Opt. Express **1**, 512–526 (2010).
[24]H. Dehghani, M. E. Eames, P. K. Yalavarthy, S. C. Davis, S. Srinivasan, C. M. Carpenter, B. W. Pogue, and K. D. Paulsen, "Near infrared optical tomography using NIRFAST: Algorithm for numerical model and image reconstruction," Commun. Numer. Methods Eng. **25**, 711–732 (2008).
[25]M. Jermyn, H. Ghadyani, M. A. Mastanduno, W. Turner, S. C. Davis, H. Dehghani, and B. W. Pogue, "Fast segmentation and high-quality three-dimensional volume mesh creation from medical images for diffuse optical tomography," J. Biomed. Opt. **18**, 86007 (2013).
[26]M. A. Naser and M. S. Patterson, "Improved bioluminescence and fluorescence reconstruction algorithms using diffuse optical tomography, normalized data, and optimized selection of the permissible source region," Biomed. Opt. Express **2**, 169–184 (2011).
[27]X. He, J. Liang, X. Wang, J. Yu, X. Qu, X. Wang, Y. Hou, D. Chen, F. Liu, and J. Tian, "Sparse reconstruction for quantitative bioluminescence tomography based on the incomplete variables truncated conjugate gradient method," Opt. Express **18**, 24825–24841 (2010).
[28]J. Pekar and M. S. Patterson, "Fabrication and characterization of phantoms with tissue-like optical properties from 500 to 700 nm," Med. Laser Appl. **25**, 147–153 (2010).
[29]G. Alexandrakis, F. R. Rannou, and A. F. Chatziioannou, "Tomographic bioluminescence imaging by use of a combined optical-PET (OPET) system: A computer simulation feasibility study," Phys. Med. Biol. **50**, 4225–4241 (2005).
[30]S. L. Jacques, "Optical properties of biological tissues: A review," Phys. Med. Biol. **58**, R37–R61 (2013).
[31]L. Cao, M. Breithaupt, and J. Peter, "Geometrical co-calibration of a tomographic optical system with CT for intrinsically co-registered imaging," Phys. Med. Biol. **55**, 1591–1606 (2010).
[32]G. Wang, W. Cong, K. Durairaj, X. Qian, H. Shen, P. Sinn, E. Hoffman, G. McLennan, and M. Henry, "*In vivo* mouse studies with bioluminescence tomography," Opt. Express **14**, 7801–7809 (2006).
[33]J. Liu, Y. Wang, X. Qu, X. Li, X. Ma, R. Han, Z. Hu, X. Chen, D. Sun, R. Zhang, D. Chen, D. Chen, X. Chen, J. Liang, F. Cao, and J. Tian, "*In vivo* quantitative bioluminescence tomography using heterogeneous and homogeneous mouse models," Opt. Express **18**, 13102–13113 (2010).
[34]R. Tuli, M. Armour, A. Surmak, J. Reyes, I. Iordachita, M. Patterson, and J. Wong, "Accuracy of off-line bioluminescence imaging to localize targets in preclinical radiation research," Radiat. Res. **179**, 416–421 (2013).
[35]R. Tuli, A. Surmak, J. Reyes, A. Hacker-Prietz, M. Armour, A. Leubner, A. Blackford, E. Tryggestad, E. M. Jaffee, J. Wong, T. L. Deweese, and J. M. Herman, "Development of a novel preclinical pancreatic cancer research model: Bioluminescence image-guided focal irradiation and tumor monitoring of orthotopic xenografts," Transl. Oncol. **5**, 77–84 (2012).
[36]M. van Herk, P. Remeijer, C. Rasch, and J. V. Lebesque, "The probability of correct target dosage: Dose-population histograms for deriving treatment margins in radiotherapy," Int. J. Radiat. Oncol., Biol., Phys. **47**, 1121–1135 (2000).
[37]B. Zhang, I. Iordachita, J. W. Wong, and K.K.-H. Wang, "Multi-projection bioluminescence tomography guided system for small animal radiation research platform," Proc. SPIE **9701**, 97010J (2016).
[38]J. Virostko, A. C. Powers, and E. D. Jansen, "Validation of luminescent source reconstruction using single-view spectrally resolved bioluminescence images," Appl. Opt. **46**, 2540–2547 (2007).
[39]G. S. Herter-Sprie, H. Korideck, C. L. Christensen, J. M. Herter, K. Rhee, R. I. Berbeco, D. G. Bennett, E. A. Akbay, D. Kozono, R. H. Mak, G. Mike Makrigiorgos, A. C. Kimmelman, and K. K. Wong, "Image-guided radiotherapy platform using single nodule conditional lung cancer mouse models," Nat. Commun. **5**, 5870:1-8 (2014).
[40]J. M. Stewart, P. E. Lindsay, and D. A. Jaffray, "Two-dimensional inverse planning and delivery with a preclinical image guided microirradiator," Med. Phys. **40**, 101709 (10pp.) (2013).
[41]M. A. Naser, M. S. Patterson, and J. W. Wong, "Algorithm for localized adaptive diffuse optical tomography and its application in bioluminescence tomography," Phys. Med. Biol. **59**, 2089–2109 (2014).
[42]J. Feng, C. Qin, K. Jia, D. Han, K. Liu, S. Zhu, X. Yang, and J. Tian, "An adaptive regularization parameter choice strategy for multispectral bioluminescence tomography," Med. Phys. **38**, 5933–5944 (2011).